Mapping and Tracking Conductivity in Memristive Nanowire Networks with Electrical Resistance Tomography

Received 24 March 2026; revised 16 April 2026; accepted 16 April 2026. Date of publication 6 May 2026; date of current version 20 May 2026.
The review of this paper was arranged by Associate Editor Alessandro M. Ferrero.
Digital Object Identifier 10.1109/OJIM.2026.3690870

Mapping and Tracking Conductivity in Memristive Nanowire Networks With Electrical Resistance Tomography

ALESSANDRO CULTRERA[1], GIANLUCA MILANO[1], CARLO RICCIARDI[2], AND LUCA CALLEGARO[1] (Member, IEEE)

[1]Istituto Nazionale di Ricerca Metrologica–INRIM, Turin, Italy
[2]Politecnico di Torino, Turin, Italy

CORRESPONDING AUTHOR: A. CULTRERA (a.cultrera@inrim.it)

This work was supported in part by the Project CAPSTAN *Quantum Electrical Italian National Capacitance Standard* through the MIUR *Progetti di Ricerca di Rilevante Interesse Nazionale* (PRIN) Bando 2020 under Grant 2020A2M33J; in part by the Project 23IND04 MetSuperCap through the European Partnership on Metrology and the European Union's (EU) Horizon Europe Research and Innovation Program; in part by the Project EMPHASIS (https://www.emphasis-supercaps.eu/) under Grant 101091997; and in part by the Project NEURONE from the European Union-Next Generation EU, M4C1 Codice Unico Progetto (CUP) I53D23003600006 through the Program PRIN 2022 under Project 20229JRTZA. The work of GIANLUCA MILANO was supported by the European Union (European Research Council (ERC), "MEMBRAIN") under Grant 101160604.

ABSTRACT In recent years, electrical resistance tomography (ERT) has been successfully applied to map the conductivity of thin-film materials and graphene. Beyond the mapping of static conductivity distribution, ERT is proposed as a new valuable tool for the characterization of memristive materials that present a dynamic behavior, where the conductivity evolves over time depending on the external stimulation. In this work, we show that ERT can provide insight into both the conductivity distribution and its time evolution in memristive metallic nanowire (NW) networks, enabling visualization of induced conductive traces in samples potentiated by means of the ERT setup itself.

INDEX TERMS Conductivity, electrical resistance tomography (ERT), memristive, nanowire (NW) networks, thin-film materials.

I. INTRODUCTION

ELECTRICAL resistance tomography (ERT) is a technique that allows for noninvasive imaging of the internal conductivity distribution of an object. ERT is the DC equivalent of EIT, representing its *impedance* counterpart [1]. Typically, ERT involves measurements of four-terminal resistance (transresistance) performed on the sample boundary [2]. Transresistance is the electrical resistance defined as the ratio between the voltage difference at a pair of contacts and the injected current at another pair. The internal conductivity distribution of the sample can be recovered by solving a regularized ill-posed inverse problem with the multiterminal measurement as the input quantity [3, Sec. 3.1]. In general, ERT can be implemented in real-time with high spatial resolution, depending on the number and position of contacts, the measurement protocols, and the used instrumentation. Typical factors affecting the ERT accuracy are the measurement noise and the inherent nonlinearity of the image reconstruction.

Recently, ERT has found application in the characterization of thin films [4] and nanostructured materials, such as graphene [2] and metallic nanowire (NW) networks [5], [6], [7]. Metallic NW networks are emerging both as novel transparent thin-film conductors with application in flexible electronics and photovoltaics [8] and as memristive materials for information processing and bio-inspired applications such as neuromorphic computing [9], [10], [11], [12], [13], [14], [15], [16], [17], with the aim of developing new computing paradigms that emulate the effectiveness of our brain. In particular, the implementation of brain-inspired computing models in self-organizing memristive NW networks relies on the emergent behavior of these systems related to resistive switching events in nanoscale network elements [18], [19], [20], [21]. The ability of leveraging both information encoding and consolidation on the same physical substrate (along with the availability of enabling experimental methods) could push a novel paradigm for *in-materia* computing.

Synthesis and optimization of such devices is strongly influenced by the intrinsic random distribution of NW junctions in self-organized networks. ERT can substantially support this field of research; in fact, beyond retrieving the electrical conductivity distribution of an NW sample, ERT can also give insight into the evolution of its topology

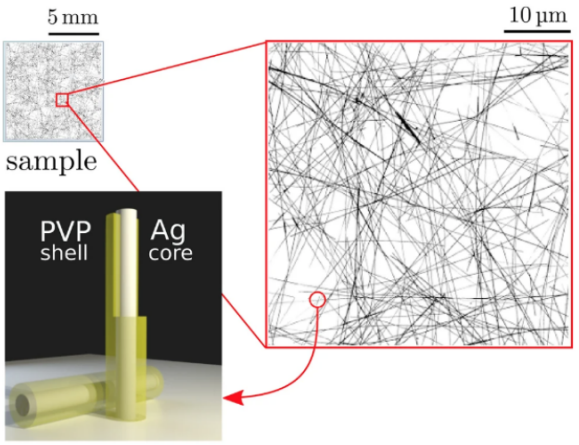

FIGURE 1. NW networks: Illustration of a 1 × 1 cm^2 sample used in this work; pictorial representation of Ag NWs with PVP shell; and a detailed SEM micrograph of a sample, showing the random self-organized NW dispersion.

associated with the stimulation of the sample. For NW networks, ERT reveals electrical connections and percolation behavior, which may differ from the NW topology [22], as individual NWs may not be electrically connected. By visualizing the NW network conductivity distribution and its time-evolution, ERT can help to optimize 1) the fabrication process and assess the impact of parameters such as NW density; 2) postprocessing treatments–e.g., encapsulation; and 3) computing input/output terminal placement. Note that EIT is unsuitable for thin-film samples because the AC current won't stay confined to the sample plane, and capacitive coupling blurs conductive paths. This frames ERT as a key enabling methodology for developing neuromorphic devices based not only on NW networks but, more generally, on self-organizing nanoscale memristive networks. This article is an extended version of the conference paper [23].

II. EXPERIMENTAL

A. NW NETWORK SAMPLES PREPARATION

Fig. 1 shows a pictorial representation of the structure of metallic NWs and scanning electron micrographs of a self-organized network of silver NWs. Metallic NWs are typically of the order of 100 μm long and 100 nm in diameter, and are coated with nanometer polymer cladding by synthesis. The investigated NW samples were synthesized starting from commercial suspended Ag NWs (Sigma-Aldrich, prod. no. 739448) of length 20–50 μm, diameter 100–130 nm, coated with about 2 nm of polyvinylpyrrolidone (PVP) and concentration of 0.5 wt% in isopropyl alcohol (IPA). The pure NW suspension was diluted 1:3 or 1:4.5 by volume in IPA and dispersed on square quartz substrates of size 1×1 cm^{-2}. The NW networks obtained exhibit an areal mass density (AMD) from 50 to 120 mg·m^{-2} (calculated). A detailed structural and chemical characterization of these types of nanostructures is reported in our previous work [7].

B. ERT MEASUREMENT SETUP

The schematic of the present ERT setup is shown in Fig. 2(a). The ERT setup used in this study accepts 1 cm^2 samples on a rigid insulating support, without the need for any lithographic step. The sample is contacted using 16 spring-mounted, gold-coated needle probes (FIXTEST GmbH, model 820.05.01.015) with a footprint of the order of 50 μm in diameter. The sample is positioned on a custom contact fixture and held in place by an engraved plastic block. A rail-mounted mechanism is actuated to land the contact array on the sample, establishing electrical contact. The contacts are positioned along the sample edge at a distance of 500 μm from it, with 2 mm spacing between adjacent contacts. The measurement unit consists of calibrated commercial instrumentation. A Keithley 2602B [24] source meter is used to energize the sample. The source meter is used as a voltage source and for source current monitoring for voltage-driven ERT (see details in Section II-C). The instrument was used with a (source) voltage range of 100 mV, a (sensing) current range of 10 mA, and an integration time of 1 NPLC. Voltage programming specifications for the considered range are (1-year, $k = 2$): resolution of 5 μV, accuracy of 0.02% of reading +250 μV, low-frequency noise of 20 μV, and a settling time of <50 μs. Similarly for the considered current range, the accuracy is 0.02% of reading +2.5 μA. An Agilent 34461A [25] voltmeter is used for voltage sensing in the range of 100 mV, with the following accuracy specifications (1-year, $k = 2$): accuracy of 0.005% of reading +350 μV. The switching matrix is an Agilent 34980A [26] multifunction unit, equipped with a reed relay board 34933A, which routes the source meter and voltmeter connections to different contact configurations according to the selected transresistance measurement sequence. The 34433A specifications are: closed-contact resistance of 1.5 Ω (+100 Ω ± 5% in-rush protection resistor), open-contact resistance >10 GΩ, and an open-close time of 500 μs. The same experimental setup used for ERT has been used to implement the van der Pauw (vdP) method for the measurement of the samples' conductivity [27], in order to compare ERT results with a more established technique. The switching matrix was programmed to perform the vdP measurements on different groups of four selected contacts among the 16 available. To estimate the accuracy of the vdP measurements, we followed the approach demonstrated in [28] where more than one vdP contact configuration is considered; in particular, in the present work, four vdP measurement configurations were used, the schematics of which are shown in Fig. 3.

The number, location, and spacing of contacts balance spatial resolution and hardware complexity: fewer contacts reduce resolution, while more increase complexity and measurement time. Placing contacts on the boundary, though less uniform in sensitivity over the sample area, is much less invasive and more suitable than other arrangements to induce and observe potentiated conductive channels across the sample.

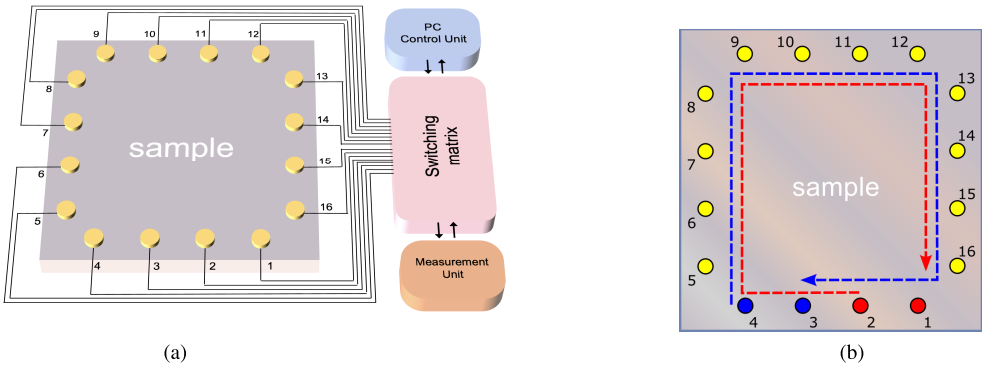

FIGURE 2. ERT implementation. (a) Schematic representation of ERT implementation with 16 contacts on a square sample (not in scale). The measurement unit includes a current/voltage source and a voltmeter for four-terminal resistance measurements; the switching matrix is a relay matrix to realize desired contact configurations. (b) Schematic of the *adjacent* stimulation/measurement protocol; red (blue) dots and arrows represent the source (sense) contacts $\{i, i+1\}$ ($\{k, k+1\}$) and sequences, respectively. For each selected pair of source contacts, a complete round of measurements at the sense pairs is carried out.

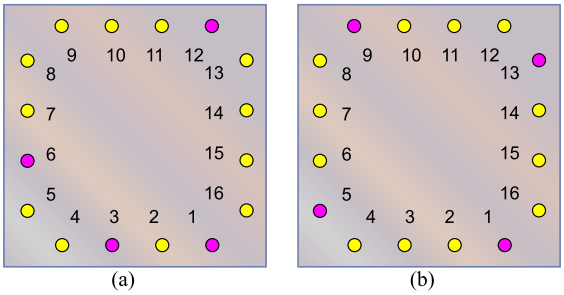

FIGURE 3. Two examples of contact configurations used for the van der Pauw measurements in the present work. (a) Magenta circles represent the used contacts $\{i, j; k, l\}$. Yellow circles represent unused contacts. The two transresistance measurements required by the vdP method are $R_\alpha = V_{k,l}/I_{i,j}$ and $R_\beta = V_{i,l}/I_{k,j}$. Configuration (b) is symmetric, which is a special case considered by the method since $R_\alpha = R_\beta$ is expected when measuring a uniform sample.

C. ERT MEASUREMENTS AND DATA REPRESENTATION

The sequence of four-terminal resistance measurements is defined by the ERT stimulation/measurement protocol. In this work, we implemented the so-called *adjacent* protocol in which the four terminal resistances are measured using adjacent pairs of contacts, as illustrated in Fig. 2(b). In this protocol, each pair $\{i, i+1\}$ of contacts acts once as the stimulation pair, while the voltage difference is measured at the other pairs $\{k, k+1\}$. With $n = 16$ contacts, the adjacent protocol yields $N = n(n-3) = 208$ transresistance measurements, with each of the 16 energizing sequences at contacts $\{i, i+1\}$ involving 13 measurements at pair contacts $\{k, k+1\}$, respectively. Independently of the applied protocol, to improve the measurement accuracy, for each contact configurations, four repeated measurements were averaged, also reversing the excitation and sensing polarity each time to minimize instrumental offsets. The total time for a complete cycle of 208 ERT measurements, including excitation and instrument switching, was approximately 50 s. Each transresistance is acquired (switching, excitation settling time, forward/reverse measurement and averaging, data recording) in about 250 ms. This gives an acquisition time for an individual map measurement of about 50 s, which is small compared with the relaxation times observed in our experiments. The measurement setup is housed in a temperature-controlled laboratory at 23.0(5) °C, with a relative humidity of about 50%, not controlled but monitored and undergoing negligible variation during the measurement time span.

Careful implementation of ERT is essential for characterizing memristive NW networks. Although their resistive switching properties are a key feature, they are also susceptible to unintended switching events during measurements when no potentiation is intended. To this aim, we carried out *voltage-driven* measurements [6], in which the sample is energized with a constant voltage that is kept under control. The applied current intensity I_{ij}, which depends on the resistance seen by the source contact pairs, and the voltage V_{kl} measured at the sensing pairs are recorded. This approach is different compared to typical ERT implementations, where a constant current is applied to the sample, often resulting in significantly high applied voltage values to the sample. Voltage-driven transresistance measurements effectively avoid unwanted sample reconfiguration due to electromigration phenomena (having a voltage threshold of the order of tens of mV) occurring at NW junctions. In fact, it has been widely reported that applied voltages exceeding a threshold of approximately 100 mV promote dissolution of Ag atoms into Ag^+ ions, which subsequently migrate under the applied electric field at NW junctions [29], [30], [31], [32]. Electromigration induces reconfiguration of the junction structure and morphology, leading to changes in junction resistance [19] and, consequently, in the NW network conductivity distribution probed by ERT. To avoid such effects, an excitation amplitude of 10 mV was selected as a conservative choice. It is worth clarifying that there is no direct evidence to rule out the possibility that local

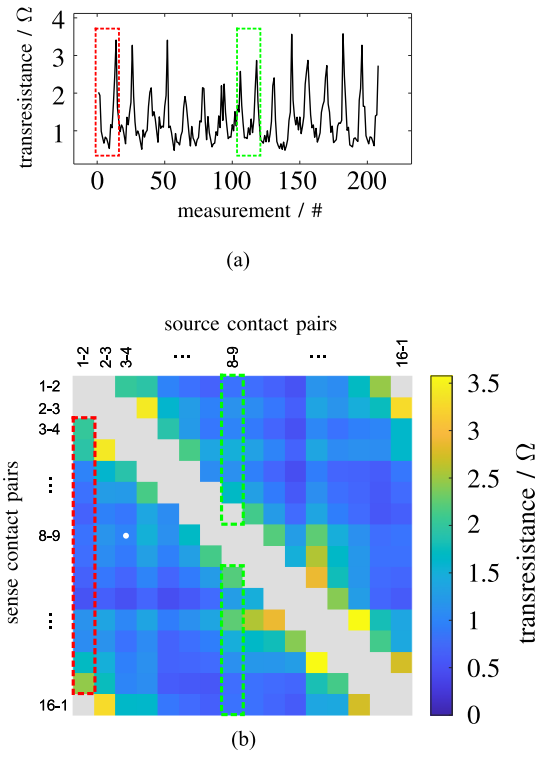

FIGURE 4. ERT measurements data representation. (a) $\mathcal{R}$ of an ERT measurement performed following the adjacent protocol with $n = 16$ contacts; the red dashed outline highlights the measurements involving contact pair $\{1, 2\}$ as source, and the other pairs $\{k, k+1\}$ as sensing pair; similarly, the green dashed outline highlights the measurements involving contact pair $\{8, 9\}$ as source. (b) Same data arranged in matrix form $\mathbf{Z}$, where columns correspond to the contact pairs used as source and the rows to the contacts used for sensing; the corresponding dashed outlines indicate the same blocks of 13 measurements highlighted in the plot of $\mathcal{R}$. The white dot marks the matrix element $Z_{3,8}$, which corresponds to the data vector element $\mathcal{R}_{3,4;8,9}$ (see text for more details).

electric fields could be sufficiently intense to modify the NW network connectivity. Nevertheless, we extensively investigated the effects of increasing the applied potential on sample alteration assessed by means of ERT. It is evident that, using the proposed voltage-driven measurements, below a certain voltage threshold, no changes are observed in both measurements reciprocity and the ERT maps (see [6], Figs. 2 and 4 and related discussion). The selected excitation voltage remained sufficient to guarantee an adequate signal-to-noise ratio. The relative standard deviation of a single transresistance measurement was on the order of 1×10^{-3} or better, comparable to the type-B uncertainty associated with instrumental accuracy, and therefore more than adequate for ERT mapping purposes.

In the presented implementation, ERT measurements data consists of two vectors $\mathcal{I}$ (energizing currents) and $\mathcal{V}$ (measured voltages) of 208 elements each, from the ratio of which the transresistance vector $\mathcal{R}$ is obtained. The elements of $\mathcal{R}$ ($R_{i,i+1;k,k+1} = V_{k,k+1}/I_{i,i+1}$) are reported in Fig. 4(a) as a plot in chronological sequence. $\mathcal{R}$ data can also be arranged as a matrix 16×16 $\mathbf{Z}$, reported in Fig. 4(b). The columns of $\mathbf{Z}$ represent the source contact pair and the rows the sense contact pairs, so each element, which is a four-terminal resistance measurement, is easily identified by the source and sense contact pairs [e.g., $Z_{3;8} \leftarrow \mathcal{R}_{3,4;,8,9}$, marked with a dot in Fig. 4(b)]. In $\mathbf{Z}$, diagonal elements (corresponding to two-terminal measurements) and the first off-diagonal elements (corresponding to three-terminal measurements) are altered by the unknown contact resistance of the current contacts. They are not necessary for the ERT reconstruction, hence not measured; the corresponding entries in the $\mathbf{Z}$ matrix are left undefined. By construction of $\mathbf{Z}$ via the adjacent ERT protocol, each contact pair serves once for sourcing but also for sensing during the corresponding reciprocal measurement. For example, during the measurement of $\mathcal{R}_{3,4;8,9}$, the pair $\{3, 4\}$ acts as current contacts, and for the reciprocal measurement $\mathcal{R}_{8,9;3,4}$, it acts as voltage contacts. The contacted sample is a passive electrical network for which the reciprocity theorem [33] applies, thus in general $\mathcal{R}_{i,j;k,l} = \mathcal{R}_{k,l;i,j}$. Therefore, within the measurement uncertainty, it should be $\mathbf{Z} = \mathbf{Z}^{\mathrm{T}}$. Although only half of $\mathbf{Z}$ carries independent information, and, in principle, ERT mapping could be performed using only half of the measurements, the redundancy provided by $\mathbf{Z}$ allows for checking the consistency with the reciprocity theorem and can point out measurement glitches. Further, in NW systems, it is possible to check if the measured sample is in a stationary condition (e.g., the sample consists of a linear, time-invariant electrical network); otherwise, it may be substantially evolving within the ERT measurement timescale, which would hinder meaningful ERT results.

D. MAPPING AND POTENTIATION OF NW NETWORK SAMPLES

To assess the conductivity distribution of NW network samples via ERT mapping, voltage stimulation at source contact pairs was set to 10 mV. The same ERT multiterminal setup was also used to potentiate memristive NW samples. In this case, a voltage in the range of 1–5 V, way larger compared to the ERT stimulation voltage used for mapping, was applied between selected pairs of contacts (usually not adjacent) for a time of the order of a few seconds to induce resistive switching of the NW junctions across the sample. The voltage amplitude range and potentiation duration were selected following previous investigations on NW resistive switching dynamics and potentiation persistence under applied voltage [5], [19]. It is worth mentioning that the tracking of memristive properties through ERT four-terminal measurements matches the concept of transmemristance reported in [34].

To recover the conductivity distribution σ, before potentiation (pristine state) and after potentiation, the corresponding ERT measurements $\mathcal{R}$ were used as input for a numerical Gauss–Newton iterative solver included in the EIDORS [35], an open source package for MATLAB. The solver minimized a Tikhonov regularized functional [36] to solve the ERT inverse problem and retrieve the σ distribution from the boundary transresistance measurements. The conductivity change $\Delta\sigma$, between pristine and post-potentiation states, was

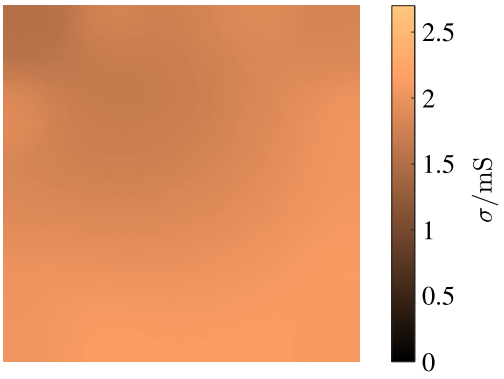

FIGURE 5. Conductivity map of the NW sample T94 in the pristine state (before potentiation).

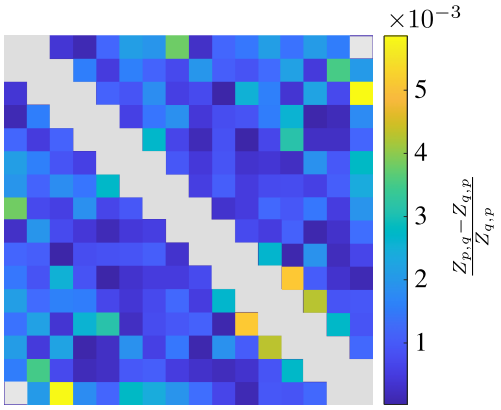

FIGURE 6. ERT measurements reciprocity assessment. The matrix reports the relative difference between matrix elements of Z that correspond to reciprocal four-terminal measurements. Gray elements correspond to elements not defined in Z.

recovered using the differential version of the same solver, in which the input data are the corresponding two ERT measurement vectors. To track the evolution of a potentiated sample during its relaxation toward the pristine state, difference maps were obtained by differential solving, subtracting each postpotentiation state of interest from the pristine state. The regularization parameter λ was selected heuristically; the parameter optimization process is discussed in Section III-C.

III. RESULTS AND DISCUSSION

To show the effectiveness of ERT for the investigation of the dynamic evolution of potentiated memristive NW networks, in the following, we present and discuss conductivity maps of NW network samples that have been subject to different potentiation schemes. To assess the memristive properties of a sample, the pristine state of the considered NW network is first mapped with ERT, then the sample is potentiated by means of the same multiterminal setup, and additional ERT measurements are carried out after potentiation to monitor the NW network evolution over time. The reciprocity of the ERT measured data is verified, and the results of ERT mapping are compared with van der Pauw conductivity measurements extracted from the same ERT data.

The ERT map of the pristine state of sample T94 is shown in Fig. 5. This map shows a fairly smooth conductivity distribution with a mean value of $\sigma_{\mathrm{ERT}} = 1.83$ mS and a variability across the sample on the order of 0.05 mS. This conductivity distribution results from the random distribution of the NW across the sample area and the resistance of each of the NW junctions; in general, NW junctions can be in a low-resistance state (LRS) if a tighter physical contact between NWs took place during the dispersion deposition. Vice versa, junctions in less intimate contact may be in a high-resistance state (HRS). The reciprocity test on sample T94 ERT data was done by calculating the relative difference between reciprocal ERT measurements configurations, hence by calculating the relative difference between the elements of Z corresponding to reciprocal measurements as $(Z_{p,q} - Z_{q,p})/Z_{p,q}$. Results shown in Fig. 6 indicate that the relative difference between reciprocal measurements is below 5.8×10^{-3}, which is of the order of the four repeated measurements' standard deviation for each of the N ERT measurements. Consequently, the sample can be considered stationary within the ERT measurement time span. Van der Pauw measurements on this sample returned a conductivity $\sigma_{\mathrm{vdP}} = 1.66 \pm 0.32$ mS. The value obtained from ERT is compatible with this estimation. The van der Pauw conductivity and resistance ratio for the symmetric measurement configuration [see Fig. 3(c)] are $\sigma_{9,13;1,5} = 1.31$ mS and $R_\alpha/R_\beta = 1.35$ respectively. The ratio $R_\alpha/R_\beta \neq 1$ for the vdP symmetric measurement configuration in Fig. 3(c) suggests a certain inhomogeneity of the sample [27], but not so heavy to be resolved by the ERT mapping. It can also be noted that the fact that $\sigma_{9,13;1,5} < \sigma_{\mathrm{ERT}}$ seems reasonable, since in the presence of sample inhomogeneity it has been reported that the vdP method tends to underestimate the sample conductivity [37]. The potentiation of the sample is now discussed. Fig. 7 reports the current flowing through the sample during potentiation across contacts {7, 10} (see inset of Fig. 7). Sample T94 was potentiated by applying a voltage of 1.5 V for 5 s. The current passing through the sample during potentiation increases by approximately 10% in 5 s. This increment occurs as more NW junctions switch from an HR) to a LRS [19]. Clear steps can be seen, corresponding to new conductive paths formed abruptly across the sample. After potentiation, the sample T94 was mapped again, and a conductive channel, extending across the stimulation contact pair, could be observed, as shown in Fig. 8, which reports the conductivity variation $\Delta\sigma$ with respect to the pristine state. The increment of local conductivity can be assigned to the potentiation of a number of NW junctions that switched from an HRS to an LRS. These variations are of the order of 3%. Reciprocity test of postpotentiation data confirmed that the sample evolution after potentiation was not so quick to hinder meaningful mapping (with relative difference between reciprocal measurements below 8.2×10^{-3}), consistent with the measurement standard deviation.

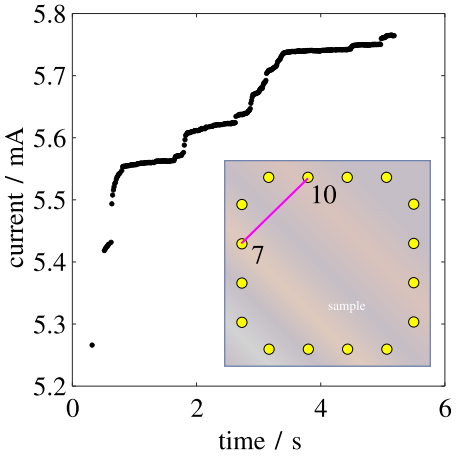

FIGURE 7. Potentiation of the NW network sample across contacts {7, 10}, 1.5 V for 5 s. The main plot reports the current injected at contact 7 as a function of time. The inset shows the schematic of the sample and contacts.

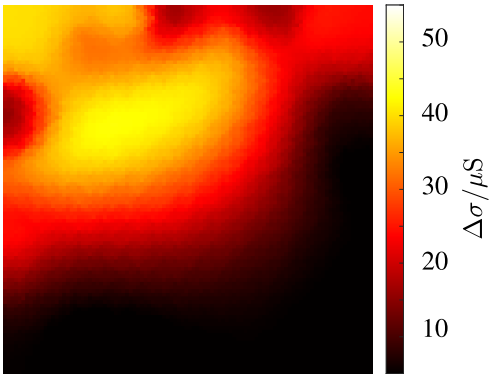

FIGURE 8. Conductivity change $\Delta\sigma$ n sampe T94 after potentiation across contacts {7, 10}.

A. REPEATABLE POTENTIATION OBSERVATION AMONG SAMPLES

It is now considered the capability of ERT to observe similar potentiation effects on different samples with the same nominal characteristics. Samples T34 and T35 were synthesized in the same batch, using a 1:3 ratio dilution of pure NW solution. The ERT maps of the pristine state of both T34 and T35 (not shown) are substantially uniform. The ERT conductivity values estimated from the maps average are $\sigma_{\mathrm{ERT,T34}} = 15.16$ mS and $\sigma_{\mathrm{ERT,T35}} = 15.34$ mS; the vdP conductivity was estimated as $\sigma_{\mathrm{vdP,T34}} = 16.72 \pm 0.52$ mS and $\sigma_{\mathrm{vdP,T35}} = 13.55 \pm 0.56$ mS, respectively (with similar considerations to T94). Both samples were potentiated by applying 3 V for 10 s across contacts {3, 10} (see Fig. 2 for contacts labels). In Fig. 9, the two maps of potentiated samples T34 and T35 are shown. The effects of the potentiation are comparable, with a conductivity increment of the order of 10%, and with straight channels connecting the potentiation contacts. This is reasonable, as we obtained fairly uniform samples, making it likely that the current paths during potentiation run straight across the potentiation contacts. Note that in the presence of a different network topology–i.e., a strongly nonuniform NW distribution over the sample, the same nominal potentiation scheme could lead to a different counter-intuitive channel shape, because of the different distribution of initial available current paths. Even though these samples have a different AMD compared to T94, it can be noted that larger potentiation effects are consistent with a higher potentiation voltage (3 versus 1.5 V) applied for a longer time (10 s versus 5 s).

B. TIME EVOLUTION OF POTENTIATED CHANNELS

As a last example of ERT applied to the characterization of memristive NW networks, the mapping of a relaxing potentiated sample is presented in the following. The sample T42 (NW precursor solution dilution of 1:4.5) was been potentiated at contacts {6, 15}, with 1.5 V for 5 s similar to T94. The top panel of Fig. 10 reports the two-terminal conductance monitored during the whole experiment at the potentiation contact pair. The sample conductance was always measured before each ERT round of measurements, using the small ERT source (reading) voltage amplitude 10 mV, and continuously during the potentiation (indicated by the red outline), when the applied voltage amplitude was 1.5 V. The initial two-terminal conductance value is approximately 1.8 mS. At 4 min, the potentiation started with the conductance increasing of about 31%. Following the potentiation, the two-terminal conductance relaxed to the initial value in about 1 h. Mapping the sample in its pristine state, the sample average conductivity was $\sigma_{\mathrm{ERT,T42}} = 3.03$ mS (comparable with $\sigma_{\mathrm{vdP,T42}} = 2.62 \pm 0.13$ mS). The bottom of Fig. 10 reports four differential ERT maps of the sample after potentiation. The maps (a)–(d) were measured at times (4, 10, 35, and 60 min), respectively. The map in (a) shows a clear potentiation of the sample, extending across the potentiation contact pair (see inset of Fig. 10). The conductivity increment along the channel is of the order of 1%, which is comparable to the results of sample T94 (similar network density). The map in (b) shows a similar channel but with lower values of $\Delta\sigma$, and is consistent with the relaxation of the sample toward the pristine state. Map in (c) indicates a substantially attenuated difference with respect to the pristine state, with a few remaining hotspots; this could indicate that some of the NW junctions did not relax from its LRS to its HRS. Finally, map in (d) shows that the spot on the right eventually returned to the HRS, while a more conductive area at the top left remained, likely due to a small irreversible change.

The overall spontaneous relaxation for this sample is related to the volatile switching mechanism observed in Ag-based memristive devices, as discussed elsewhere [9], [38].

Note that for the presented samples, undergoing potentiation conditions which induced reversible effects, the relaxation timescale (several hours) was much longer than the ERT mapping duration (approximately one minute). This means that the current ERT implementation could effectively track the evolution of potentiated samples over time while preserving measurement reciprocity and producing

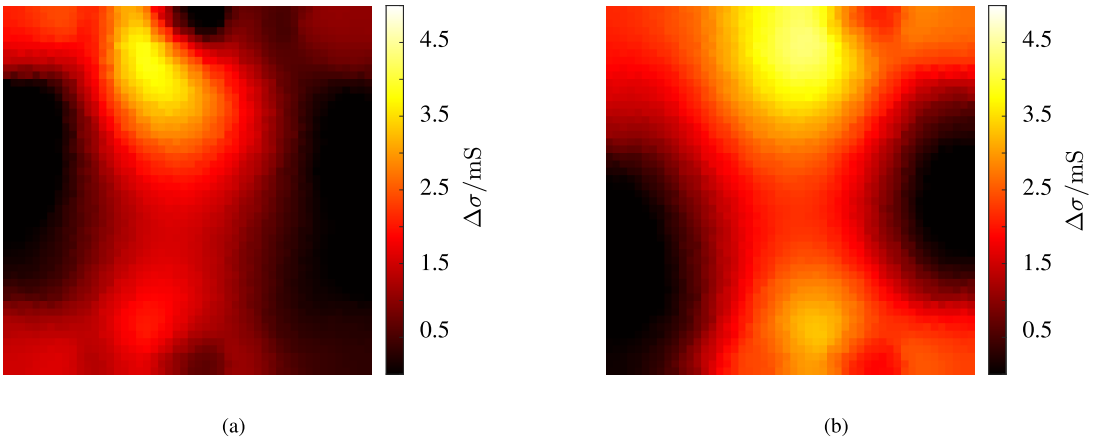

FIGURE 9. Conductivity maps of two NW samples after potentiation (3 V for 10 s) across contacts (3, 10). (a) Potentiated state conductivity map sample T34. (b) Potentiated state conductivity map sample T35.

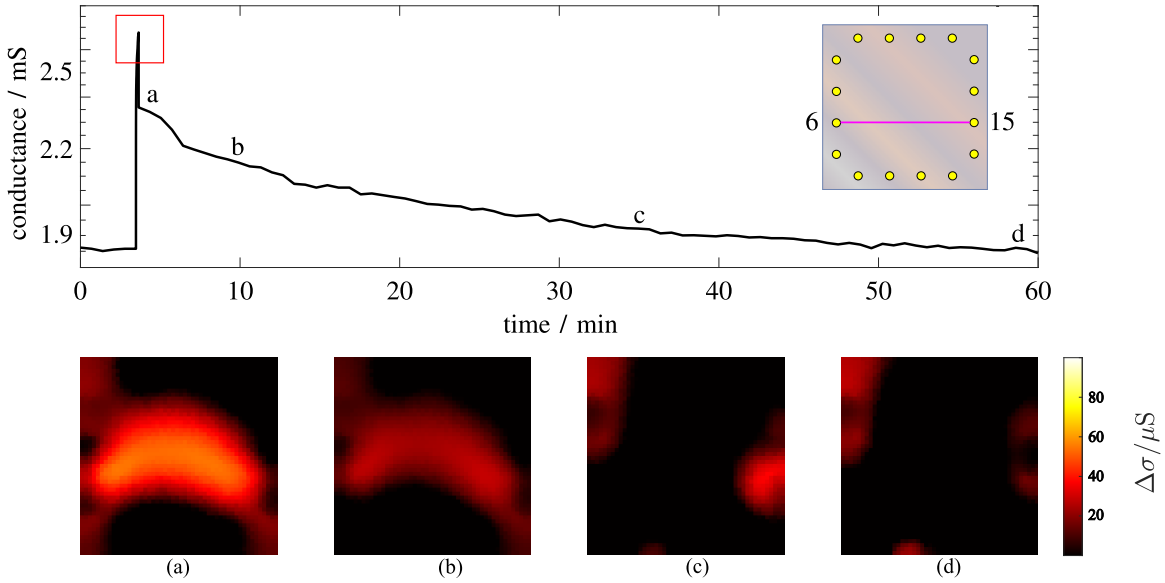

FIGURE 10. ERT mapping of the relaxation of a potentiated channel (1.5 V for 5 s) in sample T42 across contacts (6, 15). The top panel reports the two-terminal conductance of the sample measured across the contact pair used for the potentiation; at t = 4 min, the sample is potentiated (the red outline indicates the potentiation). Below, ERT differential maps acquired during the relaxation are shown: (a) first map after the potentiation, (b) maps at t = 10 min, (c) t = 35 min, and (d) t = 60 min.

meaningful conductivity maps. It is worth mentioning that, in general, faster ERT implementations can be realized, which would allow tracking the evolution of systems with faster dynamics, such as NW networks with different characteristics or other resistive switching materials).

As a final remark, concerning the validation of ERT for its application to metallic NW networks, in previous works several samples of different NW density were investigated, results were compared with established techniques (four in-line probes and the van der Pauw method) [7]. Moreover, a comparative analysis with other techniques for direct visualization of conductive pathways in self-organizing NW networks is available elsewhere (see [5, Table S2]). The validation of ERT against more established techniques and its optimization for the noninvasive characterization of self-organized NW networks opens the possibility of imaging with ERT both short- and long-term plasticity in this kind of system.

C. REGULARIZATION PARAMETER SELECTION

To further support the quantitative results presented above, this section provides the analysis of the impact of the regularization parameter λ on the stability of the map reconstruction. The selection of the regularization parameter proceeded as follows. For each sample in its pristine state and in the absence of potentiation, two consecutive ERT measurements were acquired and compared; their expected difference is zero within the limits of measurement error. To quantitatively assess the compatibility of these ERT measurement cycles, we checked that their difference was

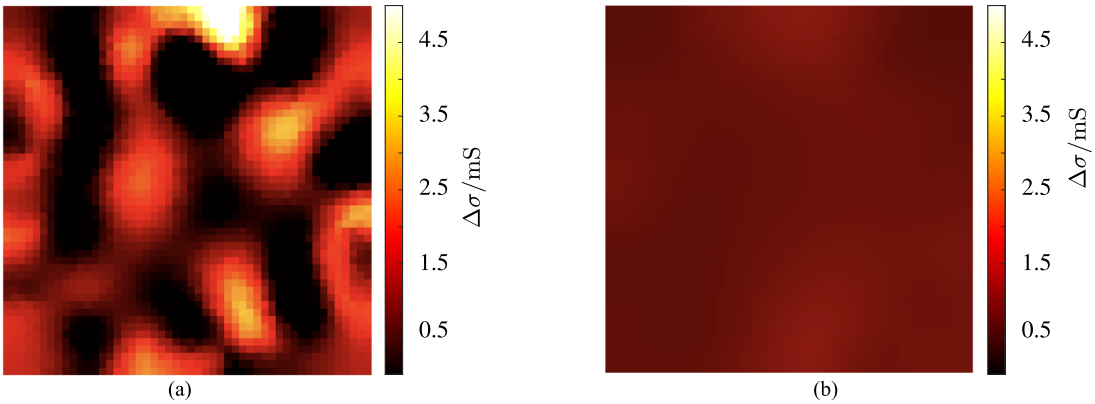

FIGURE 11. Two of the ERT null maps for sample T34 were generated to select the amount of regularization λ. The map in (a) corresponds to an under-regularized reconstruction; the map in (b) is the one corresponding to the selected value of λ for that sample. (a) $\lambda = 5 \times 10^{-3}$. (b) $\lambda = 1.35 \times 10^{-1}$.

globally of the same order as their type A uncertainty (see Section II-C). As two datasets are considered equivalent, the assumption is made that the differential ERT map obtained from these datasets is a "null map." Differential maps of these repeated ERT measurement cycles were then computed for increasing values of λ. Excessively low λ values resulted in reconstruction artifacts, whereas suitably chosen values produced "null maps" with negligible features, effectively corresponding to null reconstructions. This procedure yielded stable reconstructions of the prepotentiated state, as well as stable, non-oversmoothed reconstructions of the potentiated channels; in particular, we tested on the potentiated state the same λ values explored for reconstruction of the pristine state, and verified that the values deemed acceptable for the pristine state also provided satisfactory reconstructions for potentiated samples.

Fig. 11 shows two ERT maps of the same sample (T34, pristine state), each obtained by differential reconstruction using ERT data vectors corresponding to temporally adjacent measurement cycles.

In particular, Fig. 11(a) shows the ERT null map of sample T34, which corresponds to $\lambda = 5 \times 10^{-3}$; the map's features are reasonably attributed to reconstruction artifacts due to an insufficient regularization (with increasing artifacts amplitude for decreasing λ). On the contrary, Fig. 11(b), which corresponds to $\lambda = 1.35 \times 10^{-1}$, shows substantially zero conductivity difference, so this λ was used in the reconstruction of conductivity maps of this sample. Note that the same optimization of λ was carried out for each sample, with similar but specific values of λ.

IV. CONCLUSION

In this paper, we demonstrated that ERT can be effectively applied not only to map the conductivity distribution in NW networks but also to image and track, over time, the evolution of potentiated localized regions in memristive samples exhibiting conductivity plasticity. The experimental setup was used both to map the sample's conductivity—without triggering any unintended resistive switching—and to deliberately potentiate specific regions of the sample, subsequently mapping the resulting conductivity changes and their evolution. Moreover, the ERT results obtained on pristine-state NW samples were supported by van der Pauw measurements performed with the same experimental setup and contact fixture. Moving beyond conventional two-terminal measurements used for characterizing memristive networks, we demonstrated ERT as an enabling methodology for the controlled induction and noninvasive examination of spatially distributed changes in conductivity (plasticity) across NW networks.

ACKNOWLEDGMENT

However, the views and opinions expressed are those of the authors only and do not necessarily reflect those of the European Union or the Horizon Europe Program. Neither the European Union nor the granting authority can be held responsible for them. This article is an extended version of the 2025 IEEE International Instrumentation and Measurement Technology Conference [DOI: 10.1109/I2MTC62753.2025.11079143].

REFERENCES

[1] L. Borcea, "Electrical impedance tomography," *Inverse Problems*, vol. 18, no. 6, p. R99, 2002.
[2] A. Cultrera et al., "Mapping the conductivity of graphene with electrical resistance tomography," *Sci. Rep.*, vol. 9, no. 1, p. 10655, Jul. 2019.
[3] L. Borcea, V. Druskin, and F. G. Vasquez, "Electrical impedance tomography with resistor networks," *Inverse Problems*, vol. 24, no. 3, Jun. 2008, Art. no. 035013.
[4] A. Cultrera and L. Callegaro, "Electrical resistance tomography of conductive thin films," *IEEE Trans. Instrum. Meas.*, vol. 65, no. 9, pp. 2101–2107, Sep. 2016.
[5] G. Milano, A. Cultrera, L. Boarino, L. Callegaro, and C. Ricciardi, "Tomography of memory engrams in self-organizing nanowire connectomes," *Nature Commun.*, vol. 14, no. 1, p. 5723, Sep. 2023.
[6] A. Cultrera, G. Milano, N. De Leo, C. Ricciardi, L. Boarino, and L. Callegaro, "Recommended implementation of electrical resistance tomography for conductivity mapping of metallic nanowire networks using voltage excitation," *Sci. Rep.*, vol. 11, no. 1, pp. 1–8, Jun. 2021.
[7] G. Milano et al., "Mapping time-dependent conductivity of metallic nanowire networks by electrical resistance tomography toward transparent conductive materials," *ACS Appl. Nano Mater.*, vol. 3, no. 12, pp. 11987–11997, Dec. 2020.

[8] J. Liu, D. Jia, J. M. Gardner, E. M. J. Johansson, and X. Zhang, "Metal nanowire networks: Recent advances and challenges for new generation photovoltaics," *Mater. Today Energy*, vol. 13, pp. 152–185, Sep. 2019.

[9] G. Milano et al., "In materia reservoir computing with a fully memristive architecture based on self-organizing nanowire networks," *Nature Mater.*, vol. 21, no. 2, pp. 195–202, Feb. 2022.

[10] G. Milano, K. Montano, and C. Ricciardi, "In materia implementation strategies of physical reservoir computing with memristive nanonetworks," *J. Phys. D, Appl. Phys.*, vol. 56, no. 8, Feb. 2023, Art. no. 084005.

[11] G. Milano, F. Michieletti, D. Pilati, C. Ricciardi, and E. Miranda, "Self-organizing neuromorphic nanowire networks as stochastic dynamical systems," *Nature Commun.*, vol. 16, no. 1, p. 3509, Apr. 2025.

[12] F. Michieletti, D. Pilati, G. Milano, and C. Ricciardi, "Self-organized criticality in neuromorphic nanowire networks with tunable and local dynamics," *Adv. Funct. Mater.*, vol. 35, no. 30, Jul. 2025, Art. no. 2423903.

[13] J. Hochstetter, R. Zhu, A. Loeffler, A. Diaz-Alvarez, T. Nakayama, and Z. Kuncic, "Avalanches and edge-of-chaos learning in neuromorphic nanowire networks," *Nature Commun.*, vol. 12, no. 1, p. 4008, Jun. 2021.

[14] R. Zhu et al., "Information dynamics in neuromorphic nanowire networks," *Sci. Rep.*, vol. 11, no. 1, p. 13047, Jun. 2021.

[15] A. Loeffler et al., "Neuromorphic learning, working memory, and metaplasticity in nanowire networks," *Sci. Adv.*, vol. 9, no. 16, p. 3289, Apr. 2023.

[16] R. Zhu et al., "Online dynamical learning and sequence memory with neuromorphic nanowire networks," *Nature Commun.*, vol. 14, no. 1, p. 6697, Nov. 2023.

[17] A. Vahl, G. Milano, Z. Kuncic, S. A. Brown, and P. Milani, "Brain-inspired computing with self-assembled networks of nano-objects," *J. Phys. D, Appl. Phys.*, vol. 57, no. 50, Dec. 2024, Art. no. 503001.

[18] D. Pilati, F. Michieletti, A. Cultrera, C. Ricciardi, and G. Milano, "Emerging spatiotemporal dynamics in multiterminal neuromorphic nanowire networks through conductance matrices and voltage maps," *Adv. Electron. Mater.*, vol. 10, no. 12, Dec. 2024, Art. no. 2400750.

[19] G. Milano et al., "Brain-inspired structural plasticity through reweighting and rewiring in multi-terminal self-organizing memristive nanowire networks," *Adv. Intell. Syst.*, vol. 2, no. 8, Aug. 2020, Art. no. 2000096.

[20] E. C. Demis et al., "Atomic switch networks—Nanoarchitectonic design of a complex system for natural computing," *Nanotechnology*, vol. 26, no. 20, May 2015, Art. no. 204003.

[21] G. Milano et al., "Electrochemical rewiring through quantum conductance effects in single metallic memristive nanowires," *Nanosc. Horizons*, vol. 9, no. 3, pp. 416–426, 2024.

[22] G. Milano, E. Miranda, and C. Ricciardi, "Connectome of memristive nanowire networks through graph theory," *Neural Netw.*, vol. 150, pp. 137–148, Jun. 2022.

[23] A. Cultrera, G. Milano, C. Ricciardi, and L. Callegaro, "Electrical resistance tomography for the investigation of memristive nanowire networks," in *Proc. IEEE Int. Instrum. Meas. Technol. Conf. (I2MTC)*, May 2025, pp. 1–4.

[24] *Models 2601B, 2602B and 2604B System SourceMeter: Instrument Specifications, Rev. B ed.*, Keithley Instruments, Inc., Cleveland, OH, USA, May 2013.

[25] *Truevolt Digital Multimeters 34460A, 34461A, 34465A (6.5 digit), 34470A (7.5 digit): Data Sheet*, Keysight Technologies, Santa Rosa, CA, USA, Oct. 2019.

[26] *34980A Data Acquisition System: Data Sheet*, Keysight Technologies, Santa Rosa, CA, USA, Mar. 2024.

[27] L. J. van der Pauw, "A method of measuring the resistivity and Hall coefficient on lamellae of arbitrary shape," *Philips Tech. Rev.*, vol. 20, pp. 220–224, 1958.

[28] A. Cultrera, D. Serazio, N. Fabricius, and L. Callegaro, "New IEC standards for the measurement of sheet resistance on large-area graphene using the van der Pauw and the in-line four-point probe methods," *Measurement*, vol. 236, Aug. 2024, Art. no. 114980.

[29] G. Milano, S. Porro, I. Valov, and C. Ricciardi, "Recent developments and perspectives for memristive devices based on metal oxide nanowires," *Adv. Electron. Mater.*, vol. 5, no. 9, Sep. 2019, Art. no. 1800909.

[30] B. Stahlmecke et al., "Electromigration in gold and single crystalline silver nanowires," *Appl. Phys. Lett.*, vol. 88, no. 5, 2006, Art. no. 053122.

[31] A. T. Bellew, H. G. Manning, C. G. da Rocha, M. S. Ferreira, and J. J. Boland, "Resistance of single Ag nanowire junctions and their role in the conductivity of nanowire networks," *ACS Nano*, vol. 9, no. 11, pp. 11422–11429, Nov. 2015.

[32] J. Zhao, H. Sun, S. Dai, Y. Wang, and J. Zhu, "Electrical breakdown of nanowires," *Nano Lett.*, vol. 11, no. 11, pp. 4647–4651, Nov. 2011.

[33] M. Buttiker, "Symmetry of electrical conduction," *IBM J. Res. Develop.*, vol. 32, no. 3, pp. 317–334, May 1988.

[34] G. Milano, D. Pilati, F. Michieletti, A. Cultrera, C. Ricciardi, and E. Miranda, "Memristance and transmemristance in multiterminal memristive systems," *Sci. Rep.*, vol. 16, no. 1, p. 5271, Jan. 2026, doi: 10.1038/s41598-026-35671-7.

[35] M. Vauhkonen, W. R. B. Lionheart, L. M. Heikkinen, P. J. Vauhkonen, and J. P. Kaipio, "A MATLAB package for the EIDORS project to reconstruct two-dimensional EIT images," *Physiolog. Meas.*, vol. 22, no. 1, pp. 107–111, Feb. 2001.

[36] G. H. Golub, P. C. Hansen, and D. P. O'Leary, "Tikhonov regularization and total least squares," *SIAM J. Matrix Anal. Appl.*, vol. 21, no. 1, pp. 185–194, Jan. 1999.

[37] S. Amer, "Van der Pauw's method of measuring resistivities on lamellae of non-uniform resistivity," *Solid-State Electron.*, vol. 6, no. 2, pp. 141–145, Mar. 1963.

[38] G. Milano et al., "Self-limited single nanowire systems combining all-in-one memristive and neuromorphic functionalities," *Nature Commun.*, vol. 9, no. 1, p. 5151, Dec. 2018.